Semitransparent Organic Photovoltaics Utilizing Intrinsic Charge Generation in Non-Fullerene Acceptors

Anirudh Sharma, Nicola Gasparini, Anastasia Markina, Safakath Karuthedath, Julien Gorenflot, Han Xu, Jianhua Han, Ahmed Balawi, Wenlan Liu, Daniel Bryant, Jules Bertrandie, Joel Troughton, Sri Harish Kumar Paleti, Helen Bristow, Frederic Laquai, Denis Andrienko,* and Derya Baran*

In organic semiconductors, a donor/acceptor heterojunction is typically required for efficient dissociation of excitons. Using transient absorption spectroscopy to study the dynamics of excited states in non-fullerene acceptors (NFAs), it is shown that NFAs can generate charges without a donor/acceptor interface. This is due to the fact that dielectric solvation provides a driving force sufficient to dissociate the excited state and form the charge-transfer (CT) state. The CT state is further dissociated into free charges at interfaces between polycrystalline regions in neat NFAs. For IEICO-4F, incorporating just 9 wt% donor polymer PTB7-Th in neat films greatly boosts charge generation, enhancing efficient exciton separation into free charges. This property is utilized to fabricate donor-dilute organic photovoltaics (OPV) delivering a power conversion efficiency of 8.3% in the case of opaque devices with a metal top-electrode and an active layer average visible transmittance (AVT) of 75%. It is shown that the intrinsic charge generation in low-bandgap NFAs contributes to the overall photocurrent generation. IEICO-4F-based OPVs with limited PTB7-Th content have high thermal resilience demonstrating little drop in performance over 700 h. PTB7-Th:IEICO-4F semitransparent OPVs are leveraged to fabricate an 8-series connected semitransparent module, demonstrating light-utilization efficiency of 2.2% alongside an AVT of 63%.

1. Introduction

The performance of organic photovoltaics (OPV) is fast approaching the 20% mark,[1] largely attributed to the development of new non-fullerene acceptor (NFA) materials. In NFA-based bulk-heterojunction (BHJ) OPVs, the wide bandgap donor (D) and the narrow bandgap acceptor (A) material often exhibit complementary absorption for high light-to-current conversion. Among a wide range of reported materials, near-IR (NIR) absorbing NFA have so far been the outperforming acceptor materials in BHJ OPVs.[1,2] In contrast to the fullerene acceptors which possess Frenkel exciton binding energy of ≈1 eV, the NFA benefit from significantly lower exciton binding energy of ≈0.2–0.4 eV.[3] Moreover, NFA owing to their high light-absorption coefficients in the visible and NIR regions and long exciton diffusion lengths of up to 47 nm[4] offer tremendous potential for their application in semitransparent photovoltaics for agrivoltaics[5] and building-integrated photovoltaics (BIPV).[6]

A. Sharma, N. Gasparini, S. Karuthedath, J. Gorenflot, H. Xu, J. Han,
A. Balawi, D. Bryant, J. Bertrandie, J. Troughton, S. H. K. Paleti,
H. Bristow, F. Laquai, D. Andrienko, D. Baran
Materials Science and Engineering Program
Physical Science and Engineering Division
King Abdullah University of Science and Technology
Thuwal 23955-6900, Saudi Arabia
E-mail: denis.andrienko@mpip-mainz.mpg.de;
derya.baran@kaust.edu.sa

A. Markina, W. Liu, D. Andrienko
Max Planck Institute for Polymer Research
Ackermannweg 10, 55128 Mainz, Germany
S. Karuthedath
Institute of Materials Research
Tsinghua Shenzhen International Graduate School
Tsinghua University
Shenzhen 518055, China

Conventionally, in the case of BHJ OPVs, the D/A interface is believed to facilitate exciton dissociation by providing a driving force via the energetic offsets, type II heterojunction.[7] However, Price et. al. recently reported intrinsic charge generation in neat Y6 film without requiring a hetero-junction,[8] presenting a new paradigm for a renewed understanding of how NFA-based OPVs operate. These findings offer an exciting opportunity for understanding the underlying mechanism of intrinsic charge generation in high-performing NIR absorbing NFAs and potentially using them without or minimal amount of a donor in a BHJ. Research efforts toward developing semitransparent NFA-based OPVs have largely employed the "dilution" strategy originally introduced by Tang et al.,[9] where the amount of "donor" material in the D–A blend is significantly reduced to minimize the absorption in the visible region of the spectrum. Studies performed to develop more insights into the transport mechanism[10] in donor dilute blends with C_{60} show that the formation of large C_{60} domains leads to exciton diffusion-limited hole transfer and assists the free electron generation.[11]

Schopp et. al. reported OPVs based on PTB7-Th:COTIC-4F, achieving a power conversion efficiency (PCE) of 4% with 20 wt% PTB7-Th in the BHJ blend,[12] which resulted in an active layer average visible transmittance (AVT) of 77%. For PM6:Y6-based BHJ blends,[13] Yao et al. achieved a PCE of 10% by reducing the donor content (PM6) to only 10 wt%, where efficient hole transport was proposed to take place via the donor phase. Y6 is the only NFA material so far that has been demonstrated to intrinsically generate charges,[8,14] and owing to its ambipolar nature, it is also believed that donor material may not be required for charge transport in Y6-based OPVs.[15] This raises some fundamental questions about the role of donor molecules in the photo–physical processes and charge transport in donor-dilute OPVs, which are still not well understood.

In this work, we demonstrate that free-charge generation can occur in a range of NFA materials including IEICO, ITIC, and IDTBR families owing to spontaneous exciton splitting at room temperature. Computational studies suggest that two microscopic mechanisms facilitate charge generation in neat NFAs: a) dielectric solvation provides a driving force for an excited-to-charge transfer (CT) state transition; while, b) the polycrystalline nanostructure of the film helps the dissociation of the CT state due to different crystal fields of neighboring domains. The intrinsic charge generation in NIR absorbing NFA IEICO-4F contributes to photocurrent generation in donor-dilute semitransparent OPV devices. OPVs with only 9% PTB7-Th are shown to have remarkably improved thermal stability with almost 90% of the initial PCE retained after 700 h of thermal stress at 85 °C. Finally, a 100 × 100 mm series interconnected semitransparent OPV module with a PCE of 3.5% and AVT of 63% is fabricated, demonstrating the high compatibility of such devices with semitransparent module scale-up.

2. Results and Discussion

2.1. Photovoltaic Characterization

IEICO-4F is a low-bandgap NFA (Figure S1, Supporting Information) with peak absorption at ≈900 nm (Figure S2, Supporting Information), making it a promising candidate to be explored

Table 1. Photovoltaic parameters of IEICO-4F, IEICO-4Cl, and EH-IDTBR-based devices upon addition of different amounts of PTB7-Th.

NFA	PTB7-Th [w:w%]	J_{sc} [mA cm^{-2}]	V_{oc} [V]	FF [%]	PCE [%]
IEICO-4F	0	2.61	0.78	33	0.7
	4	6.63	0.75	55	2.7
	9	11.2	0.74	64	5.3
	17	18.6	0.71	63	8.3
	33	24.5	0.70	66	11.3
IEICO-4Cl	9	10.05	0.72	60	4.32
	17	15.91	0.72	60	6.87
	33	22.89	0.71	60	9.75
EH-IDTBR	9	5.89	1.06	56	3.52
	17	10.91	1.02	63	7.01
	33	15.80	1.01	63	10.05

for semitransparent OPVs. We first studied a model system comprising IEICO-4F blended with PTB7-Th (which absorbs visible light below 750 nm; Figures S1 and S2, Supporting Information) as an electron donor at various ratios. **Figure 1a** shows the current density–voltage (J–V) characteristics of OPVs based on 1:2 (33 w:w% donor content), 1:5 (17 w:w% donor content), and 1:10 (9 w:w% donor content) PTB7-Th:IEICO-4F weight ratio blends (**Table 1**). In agreement with previous reports, PTB7-Th:IEICO-4F blended at a ratio of 1:2 delivered a PCE of 11.3% along with a high short circuit current density (J_{sc}) of 24.5 mA cm^{-2}, open circuit voltage (V_{oc}) of 0.70 V and fill factor (FF) of 66%. Changing the D:A ratio to 1:5 and 1:10 reduces the J_{sc} to 18.6 mA cm^{-2} and 11.5 mA cm^{-2} (Figure 1b), respectively, due to the donor's reduced light harvesting capability as depicted in the external quantum efficiency (EQE) measurements reported in Figure 1c.

For varying amounts of PTB7-Th in the D–A blend, the active layer AVT was effectively tuned while retaining strong photon conversion in the NIR region. PCE values spanning from 5.3% for high AVT of 82% (9 wt% PTB7-Th) to 8.3% (AVT of 75%; 17 wt% PTB7-Th) and 11.3% (AVT of 58%; 33 wt% PTB7-Th) were achieved. PCE of 5.3% for NFA-based OPVs with active layer AVT of 82% were the highest reported so far.

The ability to generate photocurrent using only a low content of donor material in the BHJ appears to be common in NFA-based OPVs as we further demonstrate in BHJ blends of PTB7-Th with IEICO-4Cl and EH-IDTBR. In both cases, the photovoltaic properties of devices evolve consistently with those of PTB7-Th:IEICO-4F devices (Figure S3, Supporting Information), where the addition of the donor content enhances the J_{sc} (Table 1). To gain more insights into the reasonably well-performing OPVs with only 9% donor content, we study the electronic and photo–physical properties of IEICO-4F thin films and PTB7-Th:IEICO-4F based devices.

2.2. Electronic and Photo–Physical Characterization

It is noteworthy that upon diluting the PTB7-Th from 33 wt% to 9 wt% in the BHJ blend, PTB7-Th:IEICO-4F devices have a negligible change in the FF, suggesting that dilution of donor
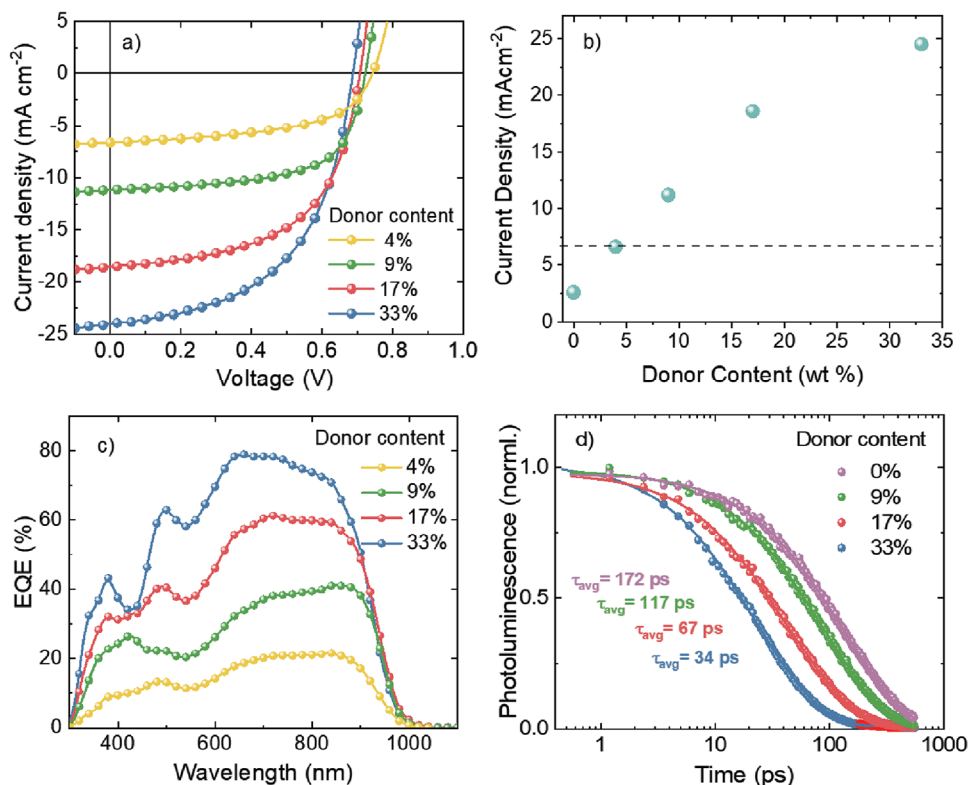
Figure 1. a) J–V characteristics, b) current density of PTB7-Th:IEICO-4F solar cells as a function of PTB7-Th (donor) content, and c) corresponding EQE measurements. d) PL dynamics averaged between 890 and 950 nm and fitted with a bi-exponential equation. Films were excited with 900 nm short-laser pulses.

material does not contribute to significant additional charge recombination pathways. This is particularly important because the D/A morphology can change[12] when reducing the content of PTB7-Th from 33% to 9%.

To probe possible recombination pathways, charge recombination in devices was studied first by analyzing the J_{sc} and V_{oc} plotted against the natural logarithm of light intensity. In the case of PTB7-Th:IEICO-4F devices with 33% PTB7-Th, J_{sc} and V_{oc} at different light intensities featured slopes of 0.91 and $1.04 \frac{kT}{q}$, respectively, not indicating strong bimolecular nor trap-assisted charge recombination. Note that the dependence of J_{sc} upon light intensity is sensitive only to the recombination of photogenerated carriers with photogenerated carriers; while, the recombination with dark carriers at the interface with transport layers dominates in OPVs.[16] Thus, a weak sublinear dependence of J_{sc} on light intensity may not be sufficient to conclusively determine bimolecular recombination, quantitatively.

However, the J_{sc} versus light intensity slope remained unchanged with donor dilution, suggesting that a) the bimolecular recombination and b) the fraction of photogenerated carriers that recombined with dark carriers did not see any significant change upon donor dilution. This further implies that the charge accumulation at the interface has not changed substantially. Schopp et al. recently argued that in donor-dilute systems, bimolecular recombination is not likely to be dominant due to re-

duced charge carrier concentration and that trap-assisted recombination is the dominant recombination pathway.[12] It is noteworthy that the observed sub-linearity of V_{oc} on light intensity was also unchanged with the donor-dilution from 33% to 9%, consistent with the trend in the FF of these devices (Figures S4 and S5, Supporting Information).

High FF values in OPVs are generally associated with a high mobility-charge carrier lifetime product. Using photo-induced charge carrier extraction by linearly increasing voltage (photo-CELIV)[17] and transient photovoltage (TPV)[18] techniques, we calculate charge carrier mobilities (μ) and charge carrier lifetimes (τ) (Figures S6 and S7, Supporting Information). Interestingly, the maximum extraction peak (t_{max}) in photo-CELIV does not change significantly as a function of donor content > 9%, implying similar effective charge carrier mobilities around 2×10^{-4} cm^2 V^{-1} s^{-1} for OPVs with 9%, 17%, and 33% PTB7-Th. The lifetimes calculated from TPV traces for the same devices are $\approx$2.3 µs in all cases, resulting in a similar $\mu\tau$ product within the range of $5.06 \pm 0.2 \times 10^{-10}$ cm^2 V^{-1}. Keeping in mind that photo-generated charges decay; thus, photovoltage decay is mostly due to their recombination with dark carriers in the vicinity of the transport layers.[16] The fact that TPV lifetime does not change with decreasing donor content also confirms that the dilution does not considerably affect the charge injection and extraction, even at the HTL/active layer interface (see equations in the Supporting Information).

On the opposite, the evolution of J_{sc} with the donor content correlates very well with the reduction of the IEICO-4F photoluminescence lifetimes, as probed by time-resolved photoluminescence spectroscopy (TRPL) and shown in Figure 1d. The IEICO-4F emission dynamics were monitored (from 850 to 950 nm) in PTB7-Th:IEICO-4F BHJ films with 9%, 17%, and 33% PTB7-Th content. The decay dynamics were fitted by a bi-exponential decay function. IEICO-4F photoluminescence decayed faster from an average of 172 ps for neat IEICO-4F down to 34 ps upon the addition of 33% PTB7-Th (Table S1, Supporting Information). This is in line with the corresponding PL quenching efficiencies where the quenching of IEICO-4F excitons is increased as a function of donor polymer PTB7-Th content (Table S2, Supporting Information).

The expected increase in the D:A interface area with the donor content can explain photoluminescence quenching, and lifetime reduction, as an exciton can readily diffuse to reach an interface, that is, approaching the case of a conventional BHJ morphology. As depicted in Table S2, Supporting Information, the calculated quenching ratios correlate well with the J_{sc} values extracted from devices, explaining the difference in charge carrier yield for these systems. However, this analysis alone fails to explain the high J_{sc} (≈ 11 mA cm^{-2}) upon the addition of only 9% PTB7-Th, considering that only one-third of the IEICO-4F excitons are quenched in this configuration. It is noteworthy that even though the J_{sc} increases almost linearly (Figure 1b) with the increase in donor content (increasing D:A interface area), there appears to be an offset where J_{sc} is non-zero even when the donor content approaches negligible amounts.

To understand this non-zero J_{sc} offset in the absence of a donor, we performed picosecond–nanosecond (ps–ns) transient absorption spectroscopy (TAS) on neat IEICO-4F film and IEICO-4F blend films to detect and identify the excited state generated upon photoexcitation (**Figure 2**). As a first step, we used reference measurement to identify the distinctive features of each species (Figure 2b). Using triplet sensitizer PtOEP for triplet excitons[18] and IEICO-4F: Copper(I) thiocyanate (CuSCN) bilayers for IEICO-4F negative charges (see also Figure S10, Supporting Information), we concluded that triplets and charges exhibited distinctive photoinduced absorption peaking at 0.9 and 1.04 eV, respectively. The exciton primarily generated upon IEICO-4F excitation; on the other hand, peaking at 1.1 eV.

TAS on neat IEICO-4F films reveals that not only singlets and triplets but also charges are formed through the evolution of the primary photo-generated excitons (normalized spectra at selected times following photoexcitation in Figure 2a). The initial pulsed excitation at 700 nm generates mostly excitons (in sub-picoseconds), with a photo-induced absorption (PA) signature peaking around 1.1 eV. This signal decays with a timescale similar to that of PL decay (Figure S8 and Table S1, Supporting Information); however, a fraction (see not-normalized spectra in Figure S9, Supporting Information) of it is converted into triplet exciton, as indicated by the distinctive triplet PA signature peaking at 0.9 eV, longer lived than the singlet excitons. In parallel, a limited quantity of charges is also generated as indicated by the PA shoulder at 1.04 eV which also corresponds to the charge-induced signature as observed in the IEICO-4F/CuSCN bilayer and the IEICO-4F:PTB7-Th blends.
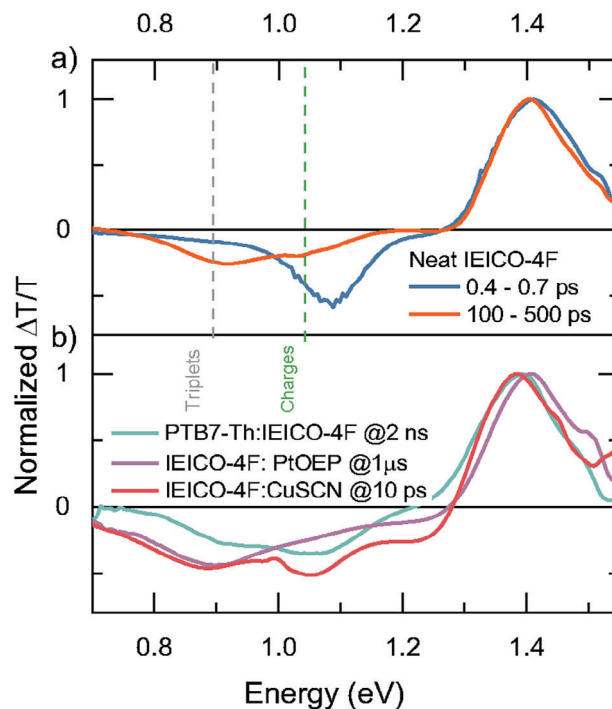

Figure 2. Normalized ps–ns (picosecond–nanosecond) TA spectra of a) neat IEICO-4F film, b) PTB7-Th:IEICO-4F (9:91) after exciting at 700 nm at 2 ns (green), IEICO-4F:PtOEP (90:10) at 1 μs (purple line), and IEICO-4F:CuSCN at 10 ps (red line). The band assignment for triplets and charges are marked by dashed lines.

Upon the addition of the donor (9 wt % PTB7-Th) to IEICO-4F, the charge band (≈ 1.04 eV) became more prominent and long-lived (green line in Figure 2b), and the ground state bleach (GSB) band (≈ 1.8 eV) was attributed to PTB7-Th (Figure S11, Supporting Information). We noted that PTB7-Th positive polaron absorption may also have a contribution close to 1.04 eV (see ref.[19] and charges in PTB7-Th:Y6 TAS signals in Figure S11d, Supporting Information for reference); and thus, may participate in the signal increase. The appearance of photo bleach of PTB7-Th (Figure S11b, Supporting Information) in the band at 1.8 eV and the presence of more long-lived charges suggest that the hole transfer channel opened upon adding a small amount of donor material. We thus conclude that intrinsic charge generation by dissociation of photo-generated singlet excitons in neat IEICO-4F domains is possible and that charge generation can be enhanced by adding a small amount of donor material.

We note that the generation in neat NFA has been reported previously in Y6[8,14b] and is confirmed by our observations. In the case of neat Y6 (Figure S12, Supporting Information), a strong photoinduced electro-absorption (EA) feature (around 1.4 eV) along with a photo-induced absorption peak around 1.35 eV, that has been attributed to charges, strongly indicates the fast generation of charges. The excitation subsequently evolves to triplets, featuring a broader GSB from 1.35 to 1.55 eV and a PA peaking around 0.9 eV (Figure S12, Supporting Information).[20]

Having now evidence of charge generation in two neat NFA materials, we check the generality of our finding by expanding our field of investigation to ITIC, ITIC-4F, ITIC-2Cl, and
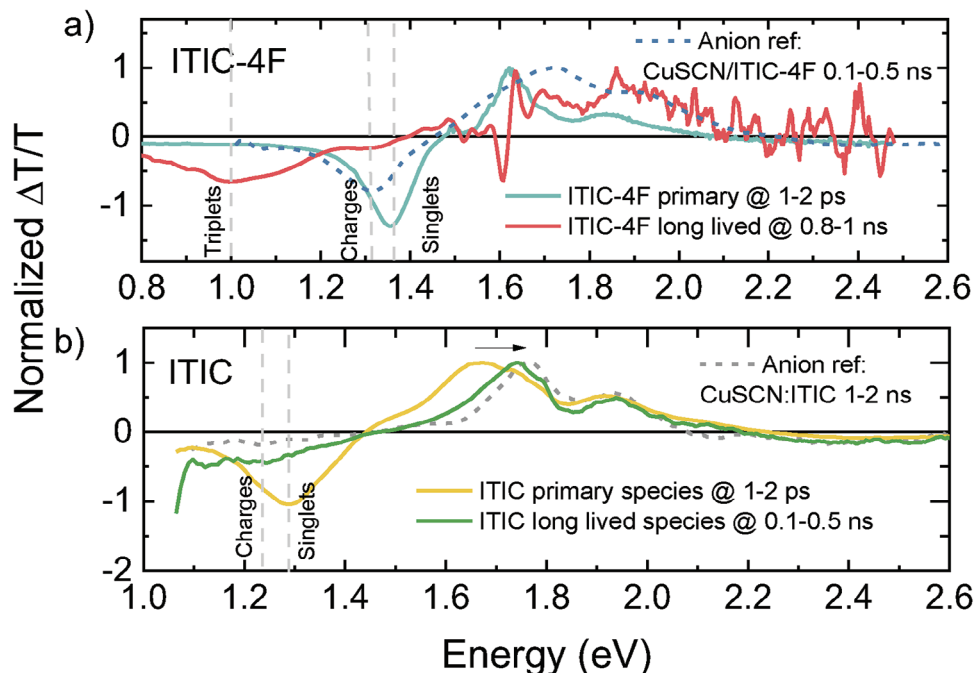
ADVANCED
SCIENCE NEWS
www.advancedsciencenews.com

ADVANCED
MATERIALS
www.advmat.de

Figure 3. Normalized ps–ns (picosecond–nanosecond) TA spectra of a) IT-4F/CuSCN and neat IT-4F films, b) ITIC/CuSCN neat ITIC after exciting at 700 nm. ps–ns TA spectra at more time delays are provided in the SI.

EH-IDTBR (Figures 3 and S13–S15, Supporting Information). Similar to IEICO-4F, the comparison of pristine ITIC and IT-4F with TAS spectra of bilayers of those materials with CuSCN (**Figure 3a**) reveals the presence of charges. In the case of IT-4F, the effect is very similar to what is observed with IEICO-4F, with the initial singlet signal (PA peaking at 1.37 eV), mostly decaying and partly evolving into triplets (PA peak at 1 eV); while only a shoulder at 1.3 eV reveals the presence of charges. Charge generation is even clearer in ITIC where the initial singlet exciton spectra seem to evolve into a spectrum almost identical to that observed with CuSCN (Figure 3b). The PA evolves from an initial peak attributed to singlets at 1.3 eV to a much broader feature, roughly maximized at 1.2 eV; while, the positive signal (GSB plus possibly stimulated emission) strongly shifts from an initial maximum around 1.65 eV to 1.72 eV after 100–500 ps.

To get some hints on what could cause the charge generation in pristine NFA films, we perturbed the molecular packing by embedding the NFA molecules in an inert matrix of polystyrene (PS), processing PS:NFA films 90:10 (w:w). TAS on those samples (PS:ITIC and PS:IT-2Cl in Figure S14, Supporting Information and PS:IT4F and PS:EHIDTBR in Figure S15, Supporting Information) indicates that the molecular packing is critical for charge formation. Indeed, the spectral evolution of the PA features that were accompanying the formation of charges and triplets in pristine NFA disappears when the molecules are insulated in the PS matrix. Instead, the PA signal does not shift all along the decay, showing that initially photogenerated species do not transform into anything else and that the excitation is just lost by decay to the ground state. A slight evolution is seen only on the GSB feature that redshifts, potentially indicating a relaxation of the excitons to the lowest energy sites.

2.3. Neat NFAs: Calculations and Characterization

TAS measurements demonstrate that charge generation in neat films requires the intervention of intermolecular, solid-state, effects. To understand how those interactions enable charge generation, we calculated the excited states energetics of a range of NFA molecules using density functional theory (DFT); we then applied polarizable force-field calculations to study how solid state interaction changes the order of those energy levels.

In details, we employed DFT and polarizable force-field calculations to evaluate energy levels of excited (EX), charge transfer (CT), and charge separated (CS) states for a range of NFAs from the IDTBR, ITIC, and IEICO family (details in Figures S16 and S17, Supporting Information and Tables S3 and S4, Supporting Information).[20] The generation of free charges is a two-step process, EX → CT and CT → CS, and both transitions should overcome Coulomb binding. In the case of the EX → CT transition, dimers in a gas phase already have a relatively small energy difference between the EX and CT states, $E_{CT} - E_{EX} \approx$ 0.2–0.7 eV, (Table S3, Supporting Information). In the solid state, where the stabilization of a CT state is much larger than that of an EX state, we find that $E_{EX} > E_{CT}$ (Table S4, Supporting Information). Hence, in spite of the strong Coulomb binding of the hole and electron in the EX state, a spontaneous dissociation into the CT state is possible.

For the CT → CS transition, the dielectric stabilizations of the CT and CS states differ by only 0.1 eV (Table S4, Supporting Information). Hence, the dielectric solvation alone cannot drive the CT state dissociation. To explain why the bound CT states still dissociate in NFAs, we evaluate solid-state ionization energies (IE) and electron affinities (EA) in polydomain morphologies of IEICO-4F as a model system, with domains of different
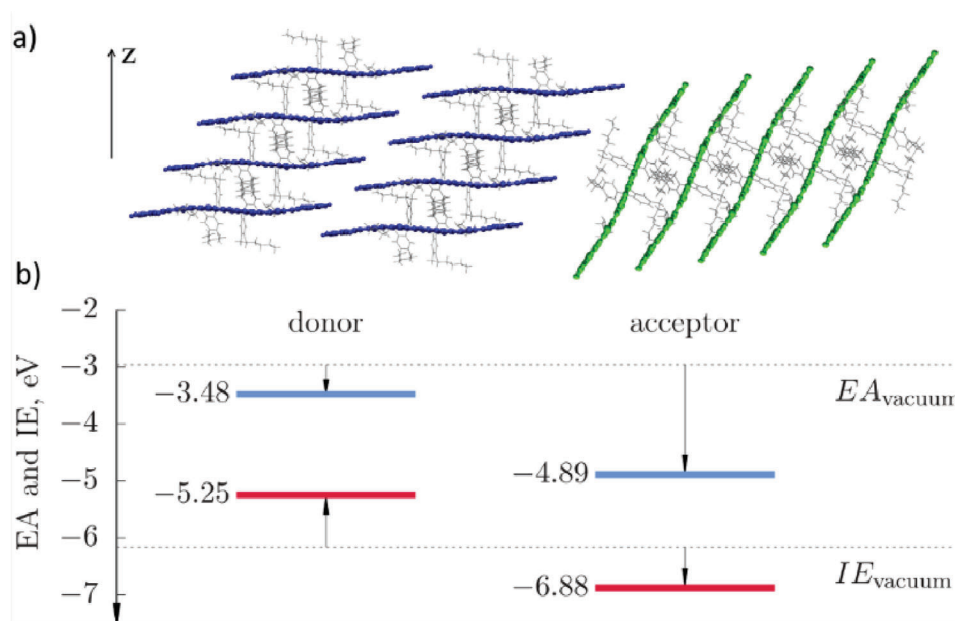
ADVANCED
SCIENCE NEWS

www.advancedsciencenews.com

**ADVANCED
MATERIALS**

www.advmat.de

Figure 4. a) Polycrystalline structure of IEICO-4F is represented by two domains: molecules parallel (left) and perpendicular (right) to the interface. b) Ionization energy (IE) and electron affinity (EA) of two films with molecular orientations corresponding to two domains. Solid-state contributions (shown as black arrows) render the interface between the domains to a type-II heterojunction.

molecular orientations, as shown in **Figure** 4a. On a molecular level, strong quadrupole moments of NFAs result in the orientation-dependent solid-state contribution to the IE and EA,[21] as shown in Figure 4b for two typical molecular orientations. In a thin film, domains of different orientations have finite sizes, as well as different orientations with respect to each other. The resulting IE and EA difference will be reduced significantly but can still be sufficient to form a type-II junction at the domain boundaries providing a required driving force for the CT to CS transition.[22]

If photo-generated charges are collected, IEICO-4F's ability to spontaneously transition to the CS state at room temperature should allow it to operate in a single-component solar cell without requiring a donor component. To verify this, we fabricated single-component IEICO-4F OPVs using zinc oxide (ZnO) as an electron transport layer (ETL) and molybdenum oxide (MoOx) as a hole transport layer (HTL) sandwiched between two electrodes. Neat IEICO-4F solar cells delivered a J_{sc} of 2.6 mA cm^{-2}, V_{oc} of 0.78 V, and a FF of 0.33 resulting in ≈0.7% efficient devices (Figure S18a, Supporting Information). Interestingly, the V_{oc} of neat IEICO-4F device is found to be 0.78 V and progressively reduces with the increase in donor content down to 0.70 V for 1:2 D/A ratio.[23] The photovoltaic parameters of these devices strongly agree with and complement the findings of TAS and the polarizable force field calculations that neat NFAs can intrinsically generate free charges.

Electrical characteristics of organic field effect transistors (OFET) based on neat IEICO-4F (Figures S18b,c and S19, Supporting Information) showed an ambipolar nature. Balanced hole and electron mobilities of 2×10^{-2} cm^2 V^{-1} s^{-1} were extracted from the saturation regime when a gate bias of either 120 V or −120 V was applied, rationalizing reasonably good photocurrent obtained from neat IEICO-4F based OPVs. We observed an analogous behavior in the case of O-IDTBR, which further confirmed the ambipolar nature of this class of acceptors (Figure S20, Supporting Information), in agreement with a recent report for Y6.[15] Similarly, space charge limited current (SCLC) measurements, which consider vertical transport in a photoactive material under dark, also demonstrated balanced hole (1.5×10^{-4} cm^2 V^{-1} S^{-1}) and electron (1.4×10^{-4} cm^2 V^{-1} S^{-1}) mobilities, in agreement with the trends observed from OFETs (Figure S21, Supporting Information). It can therefore be concluded that mobility is not the limiting factor in separating charges in neat films. The limited performance of the single-component devices is, in fact, mainly due to low FF and J_{sc} values, which reflect the limited extraction of charges. This is in accordance with the light absorption (hence simulated J_{sc}) in IEICO-4F estimated by the transfer matrix modeling, based on which only a 40 nm IEICO-4F film can be predicted to result in a PCE of 8.7% (Figure S22, Supporting Information) if IEICO-4F based single-component devices can be designed using suitable charge selective layers such that their FF is 75%. As seen from TAS measurements on neat IEICO-4F (Figure 2), the generation of triplet states is a potential cause behind the low extraction of charges, resulting in low FF and J_{sc}. Hence, the addition of a small amount of PTB7-Th enhances the absorption in the active layer as well as charge generation in IEICO-4F, suppresses triplet formation, and facilitates the hole transfer to the anode, remarkably increasing the FF and improved polymer/anode interface.[10]

2.4. Device Stability and Semitransparent Module

It has previously been shown that PTB7-Th:IEICO-4F (1:1 D:A, 50% donor content) devices exhibit severe degradation and burn-in at the initial stage of both thermal and photo-degradation.[24] This phenomenon has been ascribed to the hypo-miscibility
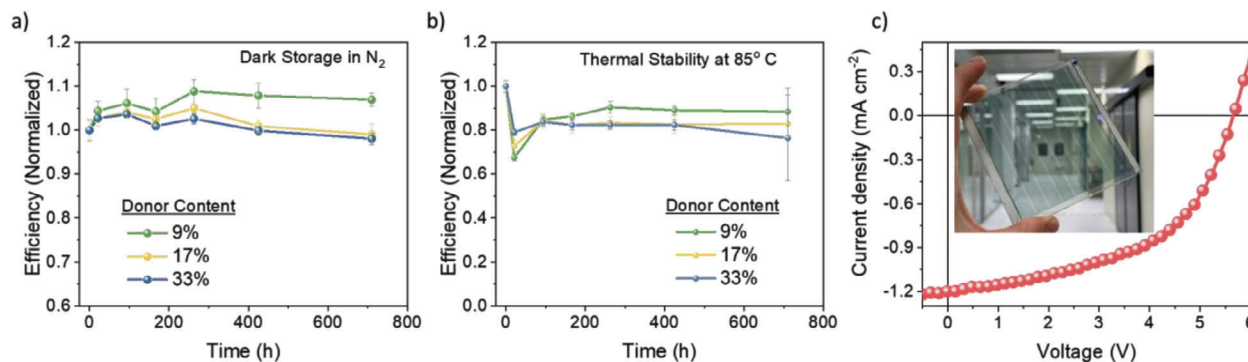
**ADVANCED
SCIENCE NEWS**

www.advancedsciencenews.com

**ADVANCED
MATERIALS**

www.advmat.de

Figure 5. Stability of PTB7-Th:IEICO-4F solar cells a) in dark and N$_2$ atmosphere b) under continuous thermal stress at 85 °C. c) J–V characteristics of semitransparent OPV module under light illumination. Inset shows a photograph of a 100 × 100 mm semitransparent OPV module.

between PTB7-Th and IEICO-4F that causes a spinodal de-mixing of the heterogeneous phases and forms trap states. The donor dilution concept benefits from reducing the visible spectrum blockage and shifting the absorption to NIR allowing semitransparency and also has the potential to eliminate any degradation pathways due to excessive changes in the donor–acceptor morphology in the BHJ.

We probed a range of PTB7-Th:IEICO-4F devices at varying levels of donor dilution and active layer AVT (Figure S23, Supporting Information), under dark and N$_2$ conditions, to determine the so-called shelf-life stability. In this test, 9% PTB7-Th-based devices showed superior shelf-life stability compared to the 17% and 33% PTB7-Th-based ones (**Figure 5a**). This suggested that photoactive layers with reduced donor content tended to quench in a more thermodynamically stable condition. These devices were also exposed to constant thermal stress at 85 °C to gauge their thermal stability, as per the International Summit on Organic Photovoltaic Stability (ISOS) protocol.[25] Over the course of more than 700 h (Figure 5b; Figure S25, Supporting Information), all devices underwent a burn-in loss in the initial 25 h and later recovered partially. OPVs with 9% PTB7-Th retained ≈90% of the initial PCE after over 700 h of thermal stress as compared to ≈76% for the 33% donor devices. It is noteworthy that the J_{sc} and FF of thermally degraded 9% PTB7-Th device were relatively the highest, as compared to 17% and 33% PTB7-Th devices. This suggests that excessive unfavorable D/A demixing due to thermal stress is limited in devices when the PTB7-Th content is reduced. Thus, in the case of donor dilute devices, a reduced amount of donor phase is expected to result in a BHJ morphology that is less prone to phase segregation, resulting in enhanced thermal stability of OPVs.

Lastly, the operational stability of OPVs with different amounts of PTB7-Th in the active layer is also studied in both inverted and conventional devices structures. Intuitively, the stability of all inverted devices (Figure S26, Supporting information) incorporating a ZnO ETL is found to be significantly worse than conventional devices (Figure S27, Supporting Information) mainly attributed to the photocatalytic effect of ZnO.[26] When a plasma lamp with a spectrum matching closely with the AM 1.5G (Figure S28, Supporting Information) is used for testing the photostability, 33% donor devices are found to have the least burn-in loss as compared to that of donor dilute devices. This suggests that unlike PTB7-Th which has earlier been shown to

be photostable,[27] IEICO-4F is relatively more prone to light-induced degradation. Donor dilute OPVs with a conventional structure and 9% donor content retain little under 60% of the initial PCE after ≈600 h of operation, as compared to 80% in the case of devices with 33% PCE after the same duration.

Notably, we also conducted photostability measurements using a metal halide lamp on the donor-dilute devices. Over the course of up to 1000 h (Figure S29, Supporting Information), 9% PTB7-Th-based devices showed negligible performance drop compared to their $T = 0$ h value, whereas higher loading of donor polymer caused photo-degradation and burn-in mainly effecting the V_{oc} and FF. This result was different from the one obtained under AM1.5G conditions using a plasma lamp (Figures S27 and S28, Supporting Information). This was mainly because the spectral characteristics of the metal halide lamp and white LED light primarily covered the wavelength range of 400–800 nm (Figure S28, Supporting Information);[28] whereas IEICO-4F primarily absorbed light in the 800–1000 nm range. Consequently, the PTB7-Th:IEICO-4F blends did not undergo their full functional response during the photostability testing using a metal halide lamp, especially for the 9% PTB7-Th-based device. It turns out that care was needed to ensure that the lamp spectra aligned with the absorption spectra of the blends when conducting photostability measurements on OSCs containing NIR-absorbing materials.[29] Nevertheless, the overall results suggest that photostable donor dilute OPVs can be achieved if both donor and acceptor materials possess good photochemical stability.

As photovoltaic modules represent an essential test bed for real-world applications, we finally demonstrate the suitability of OPVs with reduced donor content when used in photovoltaic modules. 8-series connected semitransparent OPV modules based on PTB7-Th:IEICO-4F are fabricated, where the top electrode is composed of semitransparent silver nanowires (AgNWs).[30] Figure 5c shows the solar modules as well as the light J–V characteristics. Semitransparent solar modules based on active layer with only 17% PTB7-Th deliver a PCE of 3.5%, resulting in a V_{oc} of 5.67 V, a FF of 52%, and a J_{sc} of 1.2 mA cm^{-2}, along with a geometrical fill factor of 56%. These semitransparent modules achieve an AVT of 63% (Figure S30, Supporting Information) resulting in light utilization efficiency (LUE) of 2.2%, a new Figure of merit introduced for semitransparent photovoltaics.[31] It is important to mention that the V_{oc} of the modules corresponds to the sum of V_{oc} of each individual

**ADVANCED
SCIENCE NEWS**

www.advancedsciencenews.com

**ADVANCED
MATERIALS**

www.advmat.de

sub-cell, confirming the high quality of the monolithic inter-connection of the device (for module fabrication see Supporting Information and the scheme in Figure S31, Supporting Information). OPV modules based on PTB7-Th:IEICO-4F with high AVT are highly relevant for agrivoltaics,[5] where the photosynthetically absorbed radiation (PAR) band lies between 400 and 700 nm. Application of such high-AVT OPV modules can generate electricity for efficient, and ultimately, zero-energy greenhouses, with minimal impact on the PAR band.

3. Conclusion

Combining experimental and computational tools, we demonstrate that a range of NFA materials (including IEICO-4F, ITIC, and Y6) intrinsically generate charge transfer states by dissociating singlet excitons at room temperature. This property is enabled by dielectric solvation and different crystal fields, which facilitate the transition from the excited state to the charge-transfer and charge-separated states, respectively. We rationalize this by developing IEICO-4F single-component OPV devices and confirm that charge extraction is the only limitation due to interfaces. We further develop donor-dilute semitransparent OPVs based on model system PTB7-Th:IEICO-4F. It is demonstrated that charge generation in neat NFA contributes to the overall photocurrent generation in donor-dilute devices, and the addition of a small amount of PTB7-Th to IEICO-4F is found to significantly enhance the charge generation. Opaque OPVs (with metal top-electrode) with only 9% PTB7-Th demonstrate an impressive active layer AVT of 82% and remarkable thermal stability measured for over 700 hr. Finally, semitransparent solar modules are fabricated fetching an LUE of 2.2% and V_{oc} of 5.67 V. The findings of this work are highly relevant for developing scalable semitransparent OPVs for commercial applications such as BIPV and agrivoltaic applications. The outcomes of this study also offer a compelling opportunity to revise and develop a new understanding of the working mechanisms of NFA-based OPVs, for establishing design rules for new materials, and efficient and stable devices.

4. Experimental Section

Device Fabrication and Characterization: PTB7-Th, IEICO-4F, IEICO-4Cl, EH-IDTBR, Y6, and ITIC-4F were purchased from 1-Materials Inc. All active layers were dissolved in Chlorobenzene (CB) solvent at a concentration of 20 mg mL^{-1}. Zinc oxide precursor solution was prepared by dissolving 2.4 g of zinc acetate dihydrate ($Zn(CH_3COO)_2 \cdot 2H_2O$, 99%, Sigma) and 0.647 mL of ethanolamine ($NH_2CH_2CH_2OH$, 98%, Sigma) in 30 mL of 2-methoxyethanol ($CH_3OCH_2CH_2OH$, 98%, Sigma).

Inverted OPVs were prepared as follows: pre-cleaned ITO substrates were treated by oxygen plasma treatment for 10 min to improve their work function and clearance. Subsequently, a ZnO solgel solution was spin coated on ITO substrates at 4000 rpm for 40 s and annealed at 200 °C for 10 min in air. ITO substrates coated with ZnO layer were transferred into a nitrogen-filled glovebox. The active layer solutions (40–50 nm) were spin coated at 1500–2000 rpm. MoOx (10 nm) and Ag layer (100 nm) were sequentially evaporated under a vacuum of 2×10^{-6} Torr through a shadow mask. The active area of each device was 0.1 cm^2 controlled by a shadow mask.

J–*V* measurements of solar cells were performed in the glovebox with a Keithley 2400 source meter and an Oriel Sol3A ClassAAA solar simulator calibrated to 1 sun, AM1.5 G, with a KG-5 silicon reference cell certi-

fied by Newport. In order to study the light intensity dependence of current density, a series of neutral color density filters was used. The intensity of light transmitted through the filter was independently measured via a power meter. For hole-only devices, ITO/PEDOT:PSS was used as the bottom contact and MoOx as the top contact; otherwise, for electron-only devices, ITO/ZnO was used as the bottom contact and PFN-Br/Ag as the top contact. EQE was measured using an integrated system from Enlitech, Taiwan.

Device Stability: The dark storage and thermal stability of OPVs were measured on devices with an inverted structure: ITO/ZnO/BHJ/MoOx/Ag. The devices were stored in an N$_2$ filled glove-box at room temperature (dark storage) in the dark or at constant thermal stress at 85 °C (thermal stability) and measured periodically.

Photo-stability was measured on devices with both inverted as well as conventional structure (ITO/PEDOT:PSS/BHJ/PDINO/Ag). The photo-stability results were acquired as per the ISOS-L-1 protocol with controlled temperature and humidity and samples were loaded at open circuit. The measurements were performed by loading the devices in a metal chamber with a constant N$_2$ flow and a water-cooling system, placed under the illumination of a plasma lamp (Solixon A-70-CU-2 1000 W) and a metal halide lamp where mentioned. In comparison with the commonly used light-emitting diodes (LEDs) and metal halide lamps (Figure S28, Supporting Information), the spectrum of the plasma lamp used in this study includes UV and infrared light, which closely matches the standard AM 1.5G solar irradiation and also correlates with the solar-harvesting property of PTB7-Th and IEICO-4F (Figure S28, Supporting Information). The cooling system maintained the devices at ca. 300 K to eliminate heat-induced degradation, and continuous N$_2$ flow prevented water and oxygen ingress.

Module Fabrication: To fabricate the 8-cell series interconnected module, a 100 × 100 mm sheet of ITO-coated glass was laser ablated in the pattern (Figure S31, Supporting Information) to electrically isolate strips of ITO. The active layers were deposited onto the large substrate using doctor blading. Prior to the electrode deposition, a razor blade was used to scribe through the active layers, exposing the ITO underneath (P2, Figure S31, Supporting Information). To form a transparent electrode, a suspension of silver nanowires (ClearOhm NKA710) was diluted in 2-propanol (4:1 by volume) and coated onto the glass substrate at 1 mm m^{-1} with a blade gap of 0.5 mm followed by annealing at 100 °C for 10 min under nitrogen. Finally, a third mechanical scribe was made using a razor blade to isolate the silver nanowire electrode of individual cells (P3, Figure S31, Supporting Information). The active area of the module was measured to be 56 cm^2 (Geometrical fill factor of 56%).

Absorption Measurements: Absorption spectra were acquired on a Carry 5000 UV Vis–NIR spectrophotometer by Agilent Technologies.

Photo-CELIV Measurement: In photo-CELIV measurements, the devices were illuminated with a 405 nm laser-diode. Current transients were recorded across an internal 50 Ω resistor of an oscilloscope (Agilent Technologies DSO-X 2024A). A fast electrical switch was used to isolate the cell and prevent charge extraction or sweep out during the laser pulse and the delay time. After a variable delay time, a linear extraction ramp was applied via a function generator. The ramp, which was 60 μs long and different voltages in amplitude, was set to start with an offset matching the V_{oc} of the cell for each delay time.

Transient Photovoltage Measurements (TPV): For TPV measurements, a 405 nm laser-diode was used to maintain solar cells at $\approx V_{oc}$ conditions. Laser intensity was driven using an arbitrary waveform generator Agilent 33500B. A small perturbation was induced with a second 405 nm laser diode driven by a function generator from Agilent. The intensity of the short (50 ns) laser pulse was adjusted to keep the voltage perturbation below 10 mV, typically at 5 mV. Following the pulse, the voltage decayed back to its steady state value in a single exponential decay. The characteristic decay time was determined from a linear fit to a logarithmic plot of the voltage transient and returned the small perturbation charge carrier lifetime.

Time-Resolved Photoluminescence: For time-resolved photoluminescence measurements, the samples were excited with the wavelength-tunable output of an Optical Parametric Oscillator (Radiantis Inspire

2305367 (8 of 10)

HF-100), itself pumped by the fundamental at 820 nm of a Ti:sapphire fs oscillator (Spectra Physics MaiTai eHP), yielding 100 fs pulses at a repetition rate of 80 MHz. Excitation beam after OPO was routed through pulse picker (PulseSelect, A.P.E) for repetition division. The PL of the samples was collected with an optical telescope consisting of two plano-convex lenses matched in focal length to a spectrograph (PI Spectra Pro SP2300) for wavelength dispersion and detected with a streak camera (Hamamatsu C10910) system for time resolution. The PL data was acquired in photon counting mode using the streak camera software (HPDTA) and exported to Origin Pro 2019 for further analysis.

Transient Absorption Spectroscopy (TAS): TA spectroscopy was carried out using a custom pump–probe setup. The output of a titanium:sapphire amplifier (Coherent LEGEND DUO, 4.5 mJ, 3 kHz, 100 fs) was split into three beams (2, 1, and 1.5 mJ). One of them was used to produce a white-light supercontinuum from 550 to 1700 nm by sending the 800 nm pulses through a sapphire (3 mm thick) crystal. The other two beams were used to separately pump two optical parametric amplifiers (OPA) (Light Conversion TOPAS Prime). TOPAS 1 generates tunable pump pulses, while TOPAS 2 generates signal (1300 nm) and idler (2000 nm) only. The signal from TOPAS 2 was used to produce a white-light super continuum from 400 to 1100 nm by being focused near the surface of a calcium fluoride (CaF_2) crystal which was mounted on a continuously moving stage to slow down its degradation. The pump-probe delay was adjusted by reducing the pump beam pathway between 5.12 and 2.6 m while the probe pathway length to the sample was kept constant at ≈5 m between the output of TOPAS 1 and the sample. The pump-probe path length was varied with a broadband retroreflector mounted on an automated mechanical delay stage (Newport linear stage IMS600CCHA controlled by a Newport XPS motion controller), thereby generating delays between pump and probe from −400 ps to 8 ns.

An actively Q-switched Nd:YVO4 laser (InnoLas picolo AOT) provided the excitation light (532 nm) for long delay (1 ns - 300 µs) TA experiments (for the NFA: PtOEP films), which was triggered by an electronic delay generator trigger (Stanford Research Systems DG535). The electronic delay generator triggered by the TTL sync from the Legend DUO allowed control of the delay between pump and probe with a jitter of roughly 100 ps.

Pump and probe beams were focused on the sample with the aid of proper optics. The sample (films on quartz substrates) were kept under vacuum (10^{-6} mbar) during the entire measurements. The transmitted fraction of the white light was guided to a custom-made prism spectrograph (Entwicklungsbüro Stresing) where it was dispersed by a prism onto a 512 pixels complementary metal–oxide semiconductor (CMOS) linear image sensor (Hamamatsu G11608- 512DA) for the broadband (550–1700 nm) range or a 512 pixels negative channel metal–oxide semiconductor (NMOS) linear image sensor (Hamamatsu S8381-512) for the visible (400–1100 nm) range. The probe pulse repetition rate was 3 kHz; while, the excitation pulses were mechanically chopped to 1.5 kHz (100 fs to 8 ns delays) or directly generated at 1.5 kHz frequency (1 ns to 300 µs delays); the detector array was read out at 3 kHz. Adjacent diode readings corresponding to the transmission of the sample after excitation and in the absence of an excitation pulse were used to calculate $\Delta T/T$. Measurements were averaged over several thousand shots to obtain a good signal-to-noise ratio.

The chirp induced by the transmissive optics was corrected with a custom Matlab script. The delay at which pump and probe arrived simultaneously on the sample (i.e., zero time) was determined from the point of the maximum positive slope of the TA signal rise for each wavelength.

Statistical Analysis: For *J–V* characterization of solar cells and their respective thermal and photo-stability, at least six identical cells were measured for each type of device. LabVIEW program was used to acquire and process the *J–V* data.

Supporting Information

Supporting Information is available from the Wiley Online Library or from the author.

Conflict of Interest

The authors declare no conflict of interest.

Data Availability Statement

The data that support the findings of this study are available from the corresponding author upon reasonable request.

[1] Y. Cui, Y. Xu, H. Yao, P. Bi, L. Hong, J. Zhang, Y. Zu, T. Zhang, J. Qin, J. Ren, Z. Chen, C. He, X. Hao, Z. Wei, J. Hou, *Adv. Mater.* **2021**, *33*, 2102420.

[2] J. Yuan, Y. Zhang, L. Zhou, G. Zhang, H.-L. Yip, T.-K. Lau, X. Lu, C. Zhu, H. Peng, P. A. Johnson, M. Leclerc, Y. Cao, J. Ulanski, Y. Li, Y. Zou, *Joule* **2019**, *3*, 1140.

[3] J. Bertrandie, J. Han, C. S. P. De Castro, E. Yengel, J. Gorenflot, T. Anthopoulos, F. Laquai, A. Sharma, D. Baran, *Adv. Mater.* **2022**, *34*, 2202575.

[4] Y. Firdaus, V. M. Le Corre, S. Karuthedath, W. Liu, A. Markina, W. Huang, S. Chattopadhyay, M. M. Nahid, M. I. Nugraha, Y. Lin, A. Seitkhan, A. Basu, W. Zhang, I. Mcculloch, H. Ade, J. Labram, F. Laquai, D. Andrienko, L. J. A. Koster, T. D. Anthopoulos, *Nat. Commun.* **2020**, *11*, 5220.

[5] E. Ravishankar, R. E. Booth, C. Saravitz, H. Sederoff, H. W. Ade, B. T. O'connor, *Joule* **2020**, *4*, 490.

[6] V. V. Brus, J. Lee, B. R. Luginbuhl, S.-J. Ko, G. C. Bazan, T.-Q. Nguyen, *Adv. Mater.* **2019**, *31*, 1900904.

[7] S. Karuthedath, J. Gorenflot, Y. Firdaus, N. Chaturvedi, C. S. P. De Castro, G. T. Harrison, J. I. Khan, A. Markina, A. H. Balawi, T. A. D. Peña, W. Liu, R.-Z. Liang, A. Sharma, S. H. K. Paleti, W. Zhang, Y. Lin, E. Alarousu, S. Lopatin, D. H. Anjum, P. M. Beaujuge, S. De Wolf, I. Mcculloch, T. D. Anthopoulos, D. Baran, D. Andrienko, F. Laquai, *Nat. Mater.* **2021**, *20*, 378.

[8] M. B. Price, P. A. Hume, A. Ilina, I. Wagner, R. R. Tamming, K. E. Thorn, W. Jiao, A. Goldingay, P. J. Conaghan, G. Lakhwani, N. J. L. K. Davis, Y. Wang, P. Xue, H. Lu, K. Chen, X. Zhan, J. M. Hodgkiss, *Nat. Commun.* **2022**, *13*, 2827.

[9] M. Zhang, H. Wang, H. Tian, Y. Geng, C. W. Tang, *Adv. Mater.* **2011**, *23*, 4960.

[10] D. Spoltore, A. Hofacker, J. Benduhn, S. Ullbrich, M. Nyman, O. Zeika, S. Schellhammer, Y. Fan, I. Ramirez, S. Barlow, M. Riede, S. R. Marder, F. Ortmann, K. Vandewal, *J. Phys. Chem. Lett.* **2018**, *9*, 5496.

[11] G. J. Moore, M. Causa', J. F. Martinez Hardigree, S. Karuthedath, I. Ramirez, A. Jungbluth, F. Laquai, M. Riede, N. Banerji, *J. Phys. Chem. Lett.* **2020**, *11*, 5610.

[12] N. Schopp, G. Akhtanova, P. Panoy, A. Arbuz, S. Chae, A. Yi, H. J. Kim, V. Promarak, T.-Q. Nguyen, V. V. Brus, *Adv. Mater.* **2022**, *34*, 2203796.

[13] a) N. Yao, Y. Xia, Y. Liu, S. Chen, M. P. Jonsson, F. Zhang, *ACS Appl. Energy Mater.* **2021**, *4*, 14335; b) N. Yao, J. Wang, Z. Chen, Q. Bian, Y. Xia, R. Zhang, J. Zhang, L. Qin, H. Zhu, Y. Zhang, F. Zhang, *J. Phys. Chem. Lett.* **2021**, *12*, 5039.

[14] a) G. Zhou, M. Zhang, J. Xu, Y. Yang, T. Hao, L. Zhu, L. Zhou, H. Zhu, Y. Zou, G. Wei, Y. Zhang, F. Liu, *Energy Environ. Sci.* **2022**, *15*, 3483; b) E. Saglamkaya, A. Musiienko, M. S. Shadabroo, B. Sun, S. Chandrabose, O. Shargaieva, M. G. Lo Gerfo, N. F. Van Hulst, S. Shoaee, *Mater. Horiz.* **2023**, *10*, 1825.

[15] Y. Wang, M. B. Price, R. S. Bobba, H. Lu, J. Xue, Y. Wang, M. Li, A. Ilina, P. A. Hume, B. Jia, T. Li, Y. Zhang, N. J. L. K. Davis, Z. Tang, W. Ma, Q. Qiao, J. M. Hodgkiss, X. Zhan, *Adv. Mater.* **2022**, *34*, 2206717.

[16] U. Würfel, L. Perdigón-Toro, J. Kurpiers, C. M. Wolff, P. Caprioglio, J. J. Rech, J. Zhu, X. Zhan, W. You, S. Shoaee, D. Neher, M. Stolterfoht, *J. Phys. Chem. Lett.* **2019**, *10*, 3473.

[17] A. Pivrikas, N. S. Sariciftci, G. Juska, R. Österbacka, *Prog. Photovoltaics* **2007**, *15*, 677.

[18] J. K. Jeong, H. Won Yang, J. H. Jeong, Y.-G. Mo, H. D. Kim, *Appl. Phys. Lett.* **2008**, *93*, 123508.

[19] M. A. Alamoudi, J. I. Khan, Y. Firdaus, K. Wang, D. Andrienko, P. M. Beaujuge, F. Laquai, *ACS Energy Lett.* **2018**, *3*, 802.

[20] P. A. Hume, J. M. Hodgkiss, *J.Phys. Chem. A* **2020**, *124*, 591.

[21] a) M. Schwarze, K. S. Schellhammer, K. Ortstein, J. Benduhn, C. Gaul, A. Hinderhofer, L. Perdigón Toro, R. Scholz, J. Kublitski, S. Roland, M. Lau, C. Poelking, D. Andrienko, G. Cuniberti, F. Schreiber, D. Neher, K. Vandewal, F. Ortmann, K. Leo, *Nat. Commun.* **2019**, *10*, 2466; b) Y. Fu, T. H. Lee, Y.-C. Chin, R. A. Pacalaj, C. Labanti, S. Y. Park, Y. Dong, H. W. Cho, J. Y. Kim, D. Minami, J. R. Durrant, J.-S. Kim, *Nat. Commun.* **2023**, *14*, 1870; c) S. Duhm, G. Heimel, I. Salzmann, H.

[22] Glowatzki, R. L. Johnson, A. Vollmer, J. P. Rabe, N. Koch, *Nat. Mater.* **2008**, *7*, 326.

[22] a) C. Poelking, D. Andrienko, *J. Am. Chem. Soc.* **2015**, *137*, 6320; b) C. Poelking, M. Tietze, C. Elschner, S. Olthof, D. Hertel, B. Baumeier, F. Würthner, K. Meerholz, K. Leo, D. Andrienko, *Nat. Mater.* **2015**, *14*, 434; c) C. Poelking, D. Andrienko, *J. Chem. Theory Comput.* **2016**, *12*, 4516.

[23] K. Vandewal, J. Widmer, T. Heumueller, C. J. Brabec, M. D. Mcgehee, K. Leo, M. Riede, A. Salleo, *Adv. Mater.* **2014**, *26*, 3839.

[24] a) Y. Zhu, A. Gadisa, Z. Peng, M. Ghasemi, L. Ye, Z. Xu, S. Zhao, H. Ade, *Adv. Energy Mater.* **2019**, *9*, 1900376; b) X. Song, N. Gasparini, M. M. Nahid, S. H. K. Paleti, J.-L. Wang, H. Ade, D. Baran, *Joule* **2019**, *3*, 846.

[25] a) M. O. Reese, S. A. Gevorgyan, M. Jørgensen, E. Bundgaard, S. R. Kurtz, D. S. Ginley, D. C. Olson, M. T. Lloyd, P. Morvillo, E. A. Katz, A. Elschner, O. Haillant, T. R. Currier, V. Shrotriya, M. Hermenau, M. Riede, K. R. Kirov, G. Trimmel, T. Rath, O. Inganäs, F. Zhang, M. Andersson, K. Tvingstedt, M. Lira-Cantu, D. Laird, C. Mcguiness, S. J. Gowrisanker, M. Pannone, M. Xiao, J. Hauch, et al., *Sol. Energy Mater. Sol. Cells* **2011**, *95*, 1253; b) Y. Zhang, I. D. W. Samuel, T. Wang, D. G. Lidzey, *Adv. Sci.* **2018**, *5*, 1800434.

[26] Y. Jiang, L. Sun, F. Jiang, C. Xie, L. Hu, X. Dong, F. Qin, T. Liu, L. Hu, X. Jiang, Y. Zhou, *Mater. Horiz.* **2019**, *6*, 1438.

[27] Y. Li, X. Huang, K. Ding, H. K. M. Sheriff, L. Ye, H. Liu, C.-Z. Li, H. Ade, S. R. Forrest, *Nat. Commun.* **2021**, *12*, 5419.

[28] Q. Burlingame, X. Huang, X. Liu, C. Jeong, C. Coburn, S. R. Forrest, *Nature* **2019**, *573*, 394.

[29] P. Weitz, V. M. Le Corre, X. Du, K. Forberich, C. Deibel, C. J. Brabec, T. Heumüller, *Adv. Energy Mater.* **2023**, *13*, 2202564.

[30] S. Strohm, F. Machui, S. Langner, P. Kubis, N. Gasparini, M. Salvador, I. Mcculloch, H.-J. Egelhaaf, C. J. Brabec, *Energy Environ. Sci.* **2018**, *11*, 2225.

[31] a) C. J. Traverse, R. Pandey, M. C. Barr, R. R. Lunt, *Nat. Energy* **2017**, *2*, 849; b) O. Almora, D. Baran, G. C. Bazan, C. Berger, C. I. Cabrera, K. R. Catchpole, F. Guo, J. Hauch, A. W. Y. Ho-Baillie, T. J. Jacobsson, R. A. J. Janssen, T. Kirchartz, N. Kopidakis, Y. Li, M. A. Loi, R. R. Lunt, X. Mathew, M. D. Mcgehee, J. Min, D. B. Mitzi, M. K. Nazeeruddin, J. Nelson, A. F. Nogueira, U. W. Paetzold, N.-G. Park, B. P. Rand, U. Rau, H. J. Snaith, E. Unger, et al., *Adv. Energy Mater.* **2021**, *11*, 2102526.

2305367 (10 of 10)